PAPER

Graphene prevents neurostimulation-induced platinum dissolution in fractal microelectrodes

To cite this article: Hyunsu Park *et al* 2019 *2D Mater.* **6** 035037

2D Materials

PAPER

RECEIVED
5 March 2019

REVISED
10 May 2019

ACCEPTED FOR PUBLICATION
17 May 2019

PUBLISHED
6 June 2019

Graphene prevents neurostimulation-induced platinum dissolution in fractal microelectrodes

Hyunsu Park[1], Shengjiao Zhang[2], Austin Steinman[3], Zhihong Chen[2] and Hyowon Lee[1]

[1] Weldon School of Biomedical Engineering, Birck Nanotechnology Center, Center for Implantable Devices, Purdue University, West Lafayette, IN, United States of America
[2] School of Electrical and Computer Engineering, Birck Nanotechnology Center, Purdue University, West Lafayette, IN, United States of America
[3] School of Mechanical Engineering, Purdue University, West Lafayette, IN, United States of America

E-mail: hwlee@purdue.edu

Keywords: graphene, neurostimulation, diffusion barrier, fractal electrode, Pt corrosion, microelectrodes

Supplementary material for this article is available online

Abstract

Platinum (Pt) is one of the most commonly used materials for neural interface owing to its excellent biocompatibility and good charge transfer characteristics. Although Pt is generally regarded to be a safe and inert material, it is known to undergo irreversible electrochemical dissolution during neurostimulation. The byproducts of these irreversible electrochemical reactions are known to be cytotoxic that can damage the surrounding neural substrate. With decreasing size of microelectrodes for more advanced high-density neural interfaces, there is a need for a more reliable, safe, and high-performance neurostimulating electrodes. In this work, we demonstrate that a monolayer of graphene can significantly suppress Pt dissolution while maintaining excellent electrochemical functionality. We microfabricated bare and graphene-coated Pt microelectrodes with circular and fractal designs and measured their Pt dissolution rate using inductively coupled plasma mass spectrometry. In addition, we measured changes in electrochemical characteristics of these microelectrodes before and after a prolonged stimulation period to quantify the effects of Pt dissolution and graphene protective layer. We confirm that fractal microelectrodes do have a better charge transfer performance than conventional circular designs but bare Pt fractal microelectrodes had significantly faster dissolution rate than the circular ones. When coated with monolayer of graphene, however, Pt dissolution was reduced >97% for fractal microelectrodes while they retained the superior charge transfer characteristics. The results of our work suggest that graphene can serve as an excellent diffusion barrier that can ameliorate the concerns for Pt dissolution in chronically implanted neurostimulation microelectrodes.

1. Introduction

Platinum (Pt) is widely used in neurostimulation devices as the electrode material and is regarded as the gold standard for implantable neural interface [1–6]. However, a well-known problem of using Pt, especially for a high-density neural interface with microscale electrodes, is that it can undergo irreversible electrochemical reactions during neurostimulation that can physically alter the electrode surface. Irreversible Pt dissolution can occur during neurostimulation due to cyclic formation and reduction of an oxide layer on Pt surface [7]. Moreover, Pt can react with the chloride ions during the anodic phases to form platinum chloride species that can affect cellular physiology [8–10].

Pt dissolution can have detrimental effects on the functional lifetime of neural interface by altering the geometry, the material, and the electrical properties of the microelectrode [11, 12]. Moreover, the byproduct of Pt dissolution may be toxic to the surrounding neural tissue. Pt concentration as low as 1 ppm is known to cause morphological and functional changes in neurons, and Pt concentration over 50 ppm is thought to have cytotoxic effects [13]. More recently, Wissel *et al* revealed that released Pt during the stimulation can significantly reduce mitochondrial activity and induce oxidative stress on cells [14].

Pt dissolution is thought to occur even at low current levels. In one of the classic experiments, Robblee *et al*, demonstrated a Pt dissolution rate of 0.5 μg cm^{-2} *in vivo* for 1.1 mm-diameter circular electrodes even with a low charge density of 20 μC cm^{-2}. With smaller microelectrodes, the dissolution process is expected to be accelerated. This may be problematic especially for fractal microelectrodes that are thought to have superior charge transfer capabilities than conventional circular electrodes [15–17]. Although the dissolution rate is known to be slower *in vivo* due to protein layer adsorption on the microelectrodes, the fractal designs are still expected to experience significant dissolution during neurostimulation due to their higher current density.

With the growing demand for more advanced flexible and minimally invasive neural interfaces (annual growth rate of 7%–17%) and the the increase in the number of neurological disorders (36.7% between 1990 and 2015), the use of high-density Pt microelectrodes in neurostimulation devices is likely to experience continued growth in the future [18, 19]. However, the concerns for neural interface stability due to Pt dissolution of microelectrodes may temper the excitement for these advanced microfabricated devices. Therefore, a better solution to prevent Pt dissolution is needed to ensure that these chronic neural interface remain functional for long-term usage.

In this work, we demonstrate that a graphene monolayer can be used as a protective layer that can significantly alleviate Pt-dissolution during a prolonged neurostimulation while maintaining good charge transfer characteristics. Graphene is a two-dimensional carbon sheet with a honeycomb structure. With the long range π-conjugation, graphene is widely used in electronics, energy, and biomedical applications because of its remarkable mechanical, thermal, and electrical characteristics [20–26]. Furthermore, because of its impermeability against gas and liquid, graphene is known to be an excellent diffusion barrier that can protect the surfaces of reactive metals from oxidation [27–30].

Here we microfabricated fractal and circular Pt-microelectrodes to measure their dissolution rates during a prolonged neurostimulation in a proteinaceous buffer solution. We compared the dissolution rate of the bare Pt with graphene-coated Pt (G-Pt) microelectrodes using an inductively coupled plasma-mass spectroscopy (ICP-MS) and confirmed the compositional changes using an x-ray energy dispersive spectroscopy (EDX). Furthermore, we measured the changes in electrochemical properties of various microelectrodes before and after an extended neurostimulation. We found that a graphene monolayer significantly decreased the Pt dissolution rate to negligible levels even for fractal microelectrodes with little change in their charge transfer characteristics during charge-balanced biphasic stimulation. Our results suggest that a graphene monolayer may be used to mitigate Pt-dissolution in chronically implantable neural interface devices. Moreover, these results suggest a path forward for utilizing the fractal microelectrodes for high-density neural stimulation applications (e.g. deep brain stimulation, vision prostheses, etc) without the potential reliability issues.

2. Materials and methods

2.1. Device fabrication

The circular and fractal shaped microelectrodes were designed to have identical surface area (7.854×10^{-3} mm) to investigate the impact of geometry on Pt corrosion. Pt microelectrodes array were fabricated on 500 nm film of silicon oxide by thermal oxidation of silicon wafer. Microelectrodes patterns were defined using a positive photoresist (AZ1518, MicroChem, Newton, MA, USA), which is followed by deposition of Ti adhesion layer (10 nm) and Pt layer (100 nm thick) using e-beam evaporator. The metal patterns were achieved by lift-off process using acetone. SU-8 passivation layer (1.5 μm thick) was spin-coated and patterned using photolithography.

To fabricate the G-Pt microelectrode, a monolayer of graphene (~1.7 nm-thick [31]) was grown on copper (Cu) substrate by low pressure chemical vapor deposition (CVD) at 1000 °C using methane as carbon precursor. Poly(methyl methacrylate) (PMMA) was first spin coated on the graphene layer to aid the transfer process. After curing the PMMA at 180 °C for 5 min, the Cu was etched away by $FeCl_3$ solution. The PMMA/graphene stack was washed with deionized water, then the stack was transferred onto Pt patterned substrate. PMMA was removed using acetone, the sample was cleaned with isopropyl alcohol (IPA). The transferred graphene was patterned using photolithography and reactive ion etching with oxygen plasma. Finally, SU-8 was coated and patterned for passivation layer.

2.2. Inductively coupled plasma mass spectrometry (ICP-MS)

To measure Pt dissolution rate, the 3D printed testing chamber was filled with air-saturated phosphate-buffered saline (PBS) with composition of 1.1 mM KH_2PO_4, 155 mM NaCl, 3 mM $Na_2HPO_4{\cdot}H_2O$ with pH 7.4 (ThermoFisher Scientific, Waltham, MA, USA) with 0.2 mg ml^{-1} bovine serum albumin (ThermoFisher Scientific, Waltham, MA, USA) at room temperature. The current pulses for 0.35 mC cm^{-2} were injected into the electrode at 50 Hz with a 1 ms pulse width and 1 ms inter-pulse delay. Aliquots of PBS in the testing chamber were taken every 2 h during the 10 h stimulation of each electrode type ($n = 3$, each) and measured the Pt concentration change using Thermo Element II ICP-MS (ThermoFisher Scientific, Waltham, MA, USA. Collected samples were digested using aqua regia and diluted with 4% HCl for ICP-MS analysis of Pt ion concentration.

2.3. Cyclic voltammetry and electrochemical impedance spectroscopy

CV and EIS was measured using a potentiostat (SP-200, Bio-Logic.Inc, Seyssinet-Pariset, France) with Ag/AgCl with 3M KCl (RE-1CP, ALS Co. Ltd., Tokyo, Japan), 5 mm diameter graphite counter electrode, and working electrodes on the microelectrode array. CV was measured in PBS with 0.2 mg ml^{-1} BSA. Scan rate for CV was 50 mV s^{-1} between potential range of −0.6 V and 0.8 V versus Ag/AgCl reference electrode. The cathodic charge storage capacities (CSC_c) was calculated from the overall charge storage capacity (CSC) using the following:

$$\mathrm{CSC} = \frac{1}{\nu \mathrm{A}} \int_{E_c}^{E_a} |i| \, dE \, (\mathrm{C\ cm^{-2}}) \qquad (1)$$

with the potential versus Ag/AgCl reference electrode E, the measured current i, the positive and negative potential boundaries E_a and E_c, the surface area of the microelectrode A, and the scan rate ν. For CSC_c, only the cathodic current was used for calculation. EIS were measured with the AC voltage perturbation potential of 30 mV amplitude in the frequency range from 1 to 100 kHz in PBS with BSA at room temperature.

2.4. Voltage transient with long-term stimulation

The charge-balanced biphasic current pulse was applied using a sourcemeter (2601A, Keithley, Cleveland, OH, USA) with a biased interpulse potential level to 0 V versus Ag/AgCl reference electrode. The voltage transient measurements were performed in the PBS with BSA at room temperature. To prevent DC leakage during the stimulation, an isolation capacitor (10 μF) was placed between the sourcemeter and working electrode. The pulsing was done at 50 Hz with a 1 ms pulse width and 1 ms interphase delay. The current pulses were injected into the electrode, and a data acquisition board (NI USB-6333, National Instruments, Austin, TX, USA) was used to record the voltage transient. The time delay that the applied current is completely off was measured to be approximately 50 μs, therefore, E_{mc} was estimated at 50 μs immediately after the end of the cathodic pulse. To estimate Q_{inj}, E_{mc} of each electrode was measured in the range of specific injected charge density (0.15, 0.2, 0.25, 0.3, 0.35 mC cm^{-2}). Regression function was estimated using the E_{mc} points in the injected charge density range, and Q_{inj} was calculated by the regression function.

3. Results and discussion

3.1. Design and fabrication

Leveraging our previous fractal microelectrode design, we fabricated G-Pt microelectrodes with the Vicsek fractal shape and the circular microelectrodes [17]. The fractal electrode was designed to have the same surface area with the circular microelectrode (7854 μ m^2). Figure 1(A) illustrates the overall fabrication flow. Monolayer graphene grown on copper (Cu) by CVD was transferred onto Pt-microelectrodes using the wet graphene transfer [32]. Graphene was patterned using a reactive ion etcher (RIE), which was subsequently passivated and patterned using SU-8 leaving only the microelectrodes and the contact pads exposed. Bare Pt microelectrodes with the fractal and circular designs were also fabricated as comparison.

3.2. Platinum dissolution

Figures 2(A) and (B) show bare Pt microelectrodes before and after a continuous 3 d stimulation using 0.35 mC cm^{-2} at 50 Hz, which is below the safety charge injection limit for Pt electrodes [33, 34]. Both fractal and circular design showed significant dissolution only after 3 d in a proteinaceous PBS.

Figure 2(C) compares the amount of Pt released over the stimulation period for bare and G-Pt microelectrodes with circular and fractal designs. In our previous study, the fractal microelectrodes exhibited higher current density across its surface than the circular microelectrodes for a given electrode potential [17]. With the increased current density, we predicted that the electrode dissolution may be predicted. As we expected, the bare Pt microelectrodes with fractal design showed the highest dissolution rate with 35.4 ng C^{-1} than its circular counterpart with dissolution rate of a 8.7 ng C^{-1} for 10 h-stimulation. Conversely, both fractal and circular G-Pt exhibited significant reduction in Pt dissolution rate compared to their bare Pt counterparts (1.0 ng C^{-1} for both), which supports our hypothesis that the graphene monolayer can effectively prevent dissolution as a diffusion barrier.

When comparing the total amount of lost Pt, the effectiveness of graphene monolayer in preventing dissolution becomes clearer (figure 2(D)). For fractal microelectrodes, the graphene layer reduced Pt dissolution by 97% after 10 h ($p < 0.01$, table S1). For circular microelectrodes, it reduced Pt dissolution by 88% ($p < 0.01$). For a longer stimulation period, we expect the percent reduction to be even larger for each electrode design.

To explore stability of the graphene layer on the Pt electrode surface, we performed Raman spectroscopy on G-Pt electrode surface (figure S1 (stacks.iop.org/TDM/6/035037/mmedia)). We observed the characteristic peaks for graphene monolayer before and after the neurostimulation, which suggests that graphene layer was not affected by the biphasic stimulation. We also confirmed the compositional changes using EDX (figure 3, figure S2). After 10 h stimulation, both fractal and circular bare Pt microelectrodes had higher oxygen and lower Pt contents than before the stimulation (table S2). The Pt contents were decreased by the dissolution process, which suggests that the electroactive surface may also be reduced. In contract, we saw little change in oxygen and Pt contents on G-Pt microelectrodes following the 10 h stimulation.

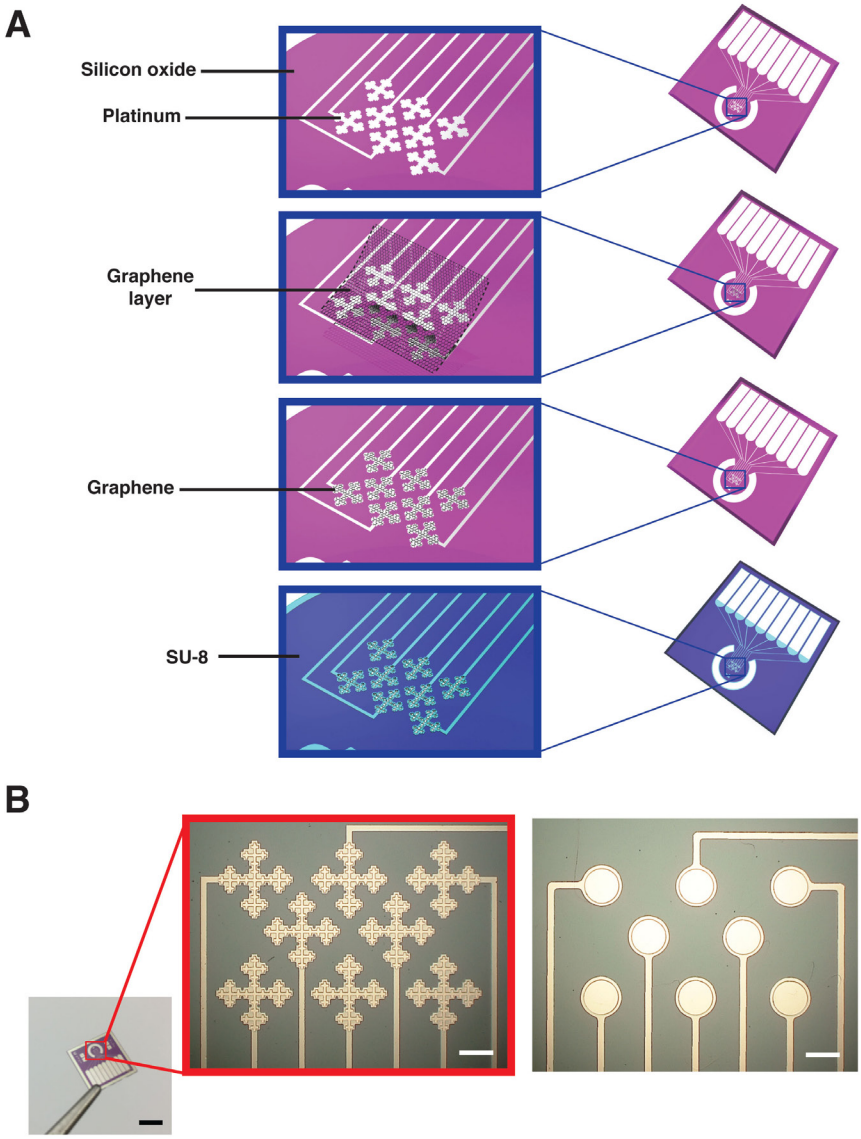

Figure 1. G-Pt microelectrodes with different shapes. (A) Fabrication process of G-Pt microelectrodes: metal patterning for electrodes and contact pads on silicon oxide on silicon wafer. Transfer the monolayer graphene. Graphene patterning for electrode sites. SU-8 patterning for the passivation layer. (B) Optical micrographs of the fabricated G-Pt microelectrodes. Scale bar =100 μm.

Although we demonstrated that the Pt dissolution may be suppressed using a graphene monolayer, we will need to further explore the robustness of this approach. The anti-corrosion properties of graphene demonstrated in other non-noble metal has shown that potential defects, cracks, or scratches on graphene could lead to a localized oxidation [35–38], which may be why we still observed some dissolution on G-Pt microelectrodes. These defects in graphene could provide a diffusion channel for molecules such as O_2 and H_2O through the graphene–metal interface [39–41] and the space between graphene–metal interface may act as a 2D container for Faradaic reactions [42–44]. When the coupling is strong, the density of states of graphene gets modified and changes from the Dirac cone dispersion to a more conventional parabolic dispersion [45]. As such, we suspect that different substrate metals have varying degrees of coupling interaction with graphene, which can impact various electrochemical reactions including corrosion and charge transfer process. Therefore, a careful consideration of metallic substrate may be necessary to avoid generation of potentially harmful electrochemical byproducts that can compromise the neural interface over long-term.

One way to mitigate graphene defects is to use multi-layer graphene. However, additional graphene layers may increase overall electrode impedance and reduce charge transfer performance of these stimulating microelectrodes. Nevertheless, it would be informative to demonstrate the impact of monolayer and multi-layer G-Pt microelectrodes using *in vitro* and *in vivo* models. Our results show that G-Pt microelectrodes had only 0.019 ng ml^{-1} of dissolution after 10 h stimulation. In previous studies, >1.6 μg ml^{-1} of dissolved Pt was required to induce cell death [45]. Although it would require 35 d of continuous stimulation to generate such large concentration Pt from

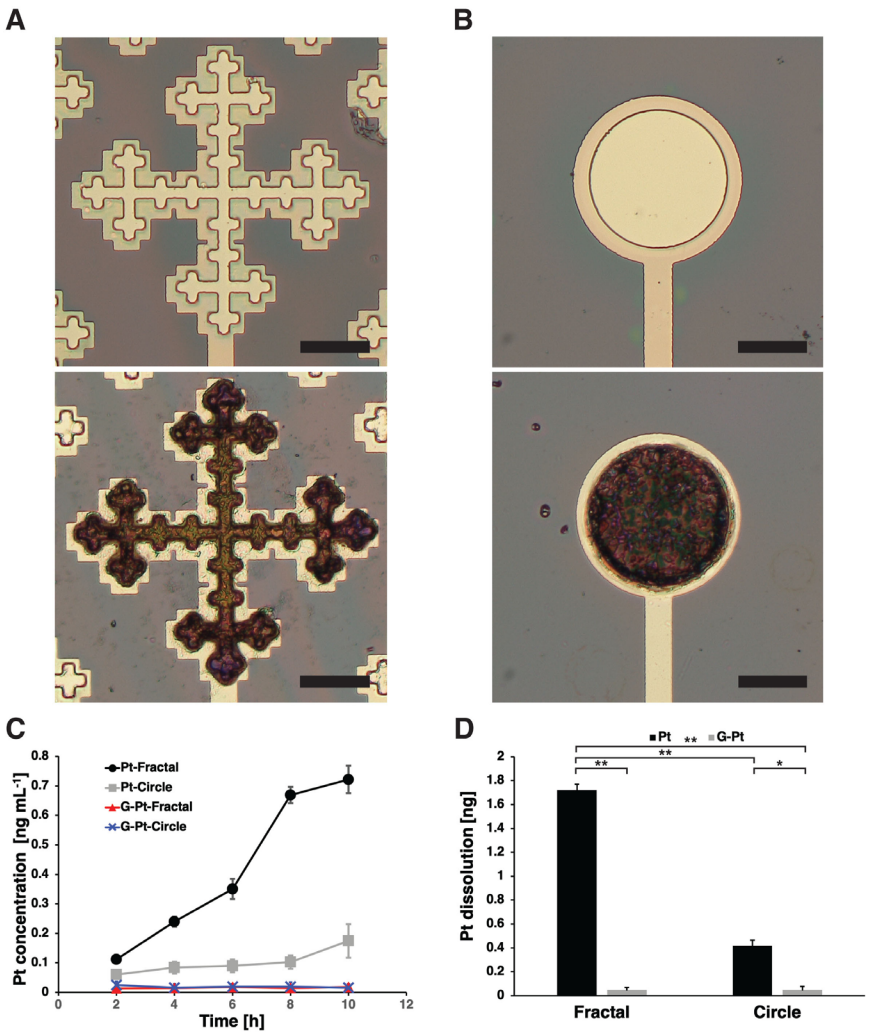

Figure 2. Pt microelectrodes dissolution. (A) Representative optical image of Pt microelectrode with the fractal design before (top) and after (bottom) 3 d stimulation. Scale bar $=50\ \mu$m. (B) Optical images of circular Pt microelectrodes before (top) and after (bottom) 3 d stimulation. Scale bar $=50\ \mu$m. (C) Pt concentration in PBS from the fractal and circle microelectrodes with Pt and G-Pt. (D) Total Pt dissolution for 10 h-stimulation, which showed statistically significant reduction for both fractal and circular microelectrodes ($*$ for $p < 0.05$, and $**$ for $p < 0.01$).

monolayer G-Pt, it would be interesting to see how multi-layer G-Pt microelectrodes would perform.

3.3. Cyclic voltammetry

To investigate the impact of Pt dissolution on the electrochemical performance and the CSC_c of these microelectrodes, we performed CV measurements on bare Pt and G-Pt microelectrodes with different designs. Figures 4(A) and (B) show a substantial decrease in oxidation and reduction peaks following a 10 h of stimulation using bare Pt microelectrodes with either fractal or circular design. These results suggest that the bare Pt microelectrodes not only demonstrate physical changes (figure 2) but they also undergo substantial changes to their electrochemical characteristics after only a 10 h of continuous stimulation. In comparison, G-Pt microelectrodes demonstrated little change in CV after the same treatment (figures 4(C) and (D)). Compared to the bare Pt microelectrodes, G-Pt ones showed substantially decreased Faradaic reaction peaks, which supports our hypothesis that the graphene layer can significantly reduce Pt dissolution by impeding the diffusion of oxidative species.

The CSC_c measures the total amount of charge available for a single cathodic stimulation pulse, which is an indication of the cathodic charge injection capacity. Using one-way ANOVA with Tukey's HSD post-hoc test, we compared the CSC_c of each microelectrode before and after the 10 h stimulation (figure 4(E)). The CSC_c of bare Pt microelectrodes decreased significantly after the 10 h stimulation ($p < 0.01$). As expected, the fractal microelectrodes showed a more significant CSC_c decrease than the circular microelectrodes.

However, G-Pt microelectrodes showed little changes in CSC_c before and after the stimulation. This further supports our hypothesis that the graphene layer can provide protection against Pt dissolution and prevent changes in charge transfer characteristics. Although G-Pt microelectrodes had smaller CSC_c than bare Pt microelectrodes, which is most likely due to the

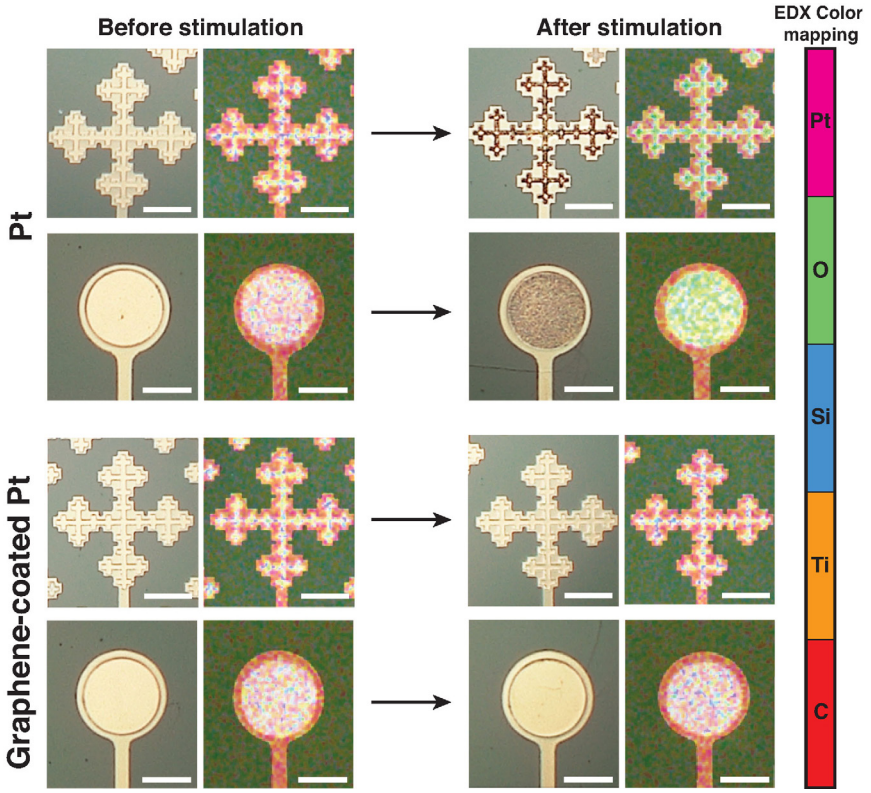

Figure 3. Optical images and the corresponding EDX color map of Pt and G-Pt microelectrodes. In the EDX image, pink, green, blue, orange, red dots indicate the presence of Pt, oxide, silicon, titanium, and carbon, respectively. Scale bar =50 μm. Note the change in coloration in both optical and EDX images that suggests change in electrode material.

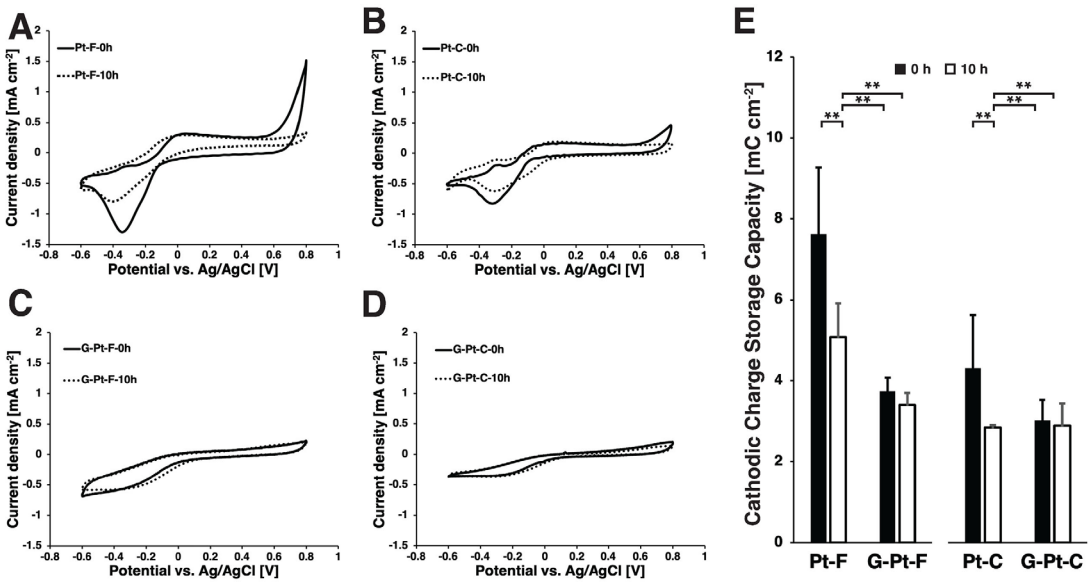

Figure 4. CV of Pt and G-Pt microelectrodes. (A) CV of fractal Pt microelectrodes before and after the stimulation. (B) CV of the circular Pt microelectrodes . (C) Cyclic voltammetry measurements on the fractal G-Pt microelectrodes. (D) Cyclic voltammetry measurements on the circular G-Pt microelectrodes. (E) CSC of each electrode ($n = 5$ for each). Note that ANOVA showed statistically significant differences between electrodes ($**, p < 0.01$).

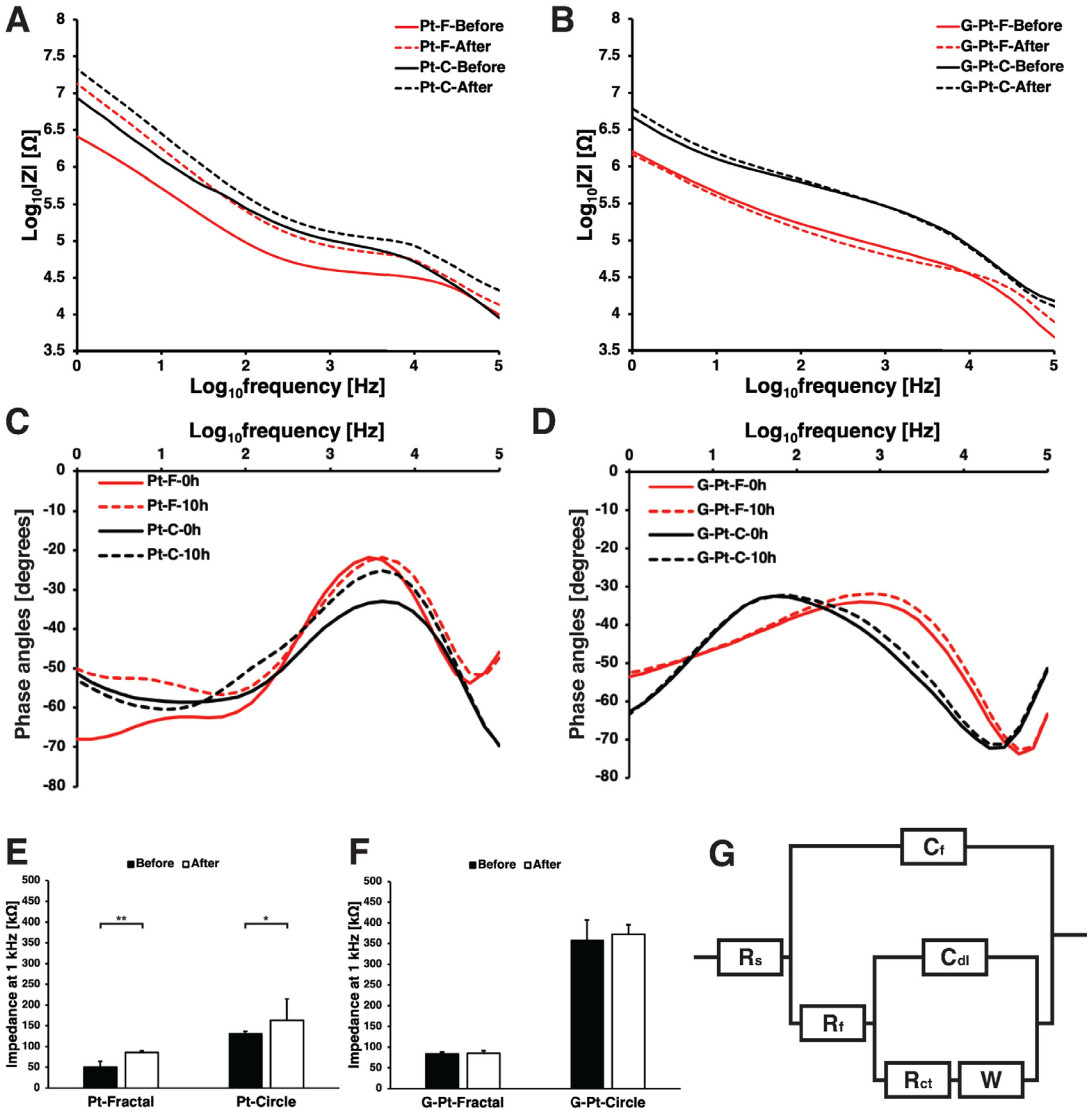

Figure 5. Electrochemical impedance spectroscopy. (A) Impedance responses of the bare Pt microelectrodes with different shapes before and after the stimulation. (B) Impedance responses of the G-Pt microelectrodes. (C) Phase angle versus frequency of the Pt microelectrodes. (D) Phase angle versus frequency of the G-Pt microelectrodes. (E) Impedance of Pt microelectrodes at 1 kHz (∗ for $p < 0.05$, and ∗∗ for $p < 0.01$). (F) Impedance of G-Pt at 1 kHz. (G) Equivalent circuit model for each electrode in PBS with BSA.

reduction in Faradaic charge transfer, the improved stability in CSC_c suggest G-Pt may be a better neural interface for chronic implantation.

3.4. Electrochemical impedance spectroscopy

Next, we performed EIS to evaluate the changes in microelectrode impedance following the stimulation ($n = 5$, each). Figure 5(A) shows the impedance spectra of the bare Pt and G-Pt microelectrodes before and after the stimulation. Throughout the entire frequency range, the impedance of bare Pt electrodes increased (figure 5(A)) . In contrast, we observed relatively small differences in the G-Pt microelectrodes (figure 5(B)).

The phase responses of Pt and G-Pt microelectrodes had different shapes, which demonstrate the impacts of electrode design and graphene coating (figures 5(C) and (D)). Compared to the bare Pt microelectrodes, G-Pt microelectrodes showed relatively small change in phase responses before and after the stimulation. When comparing the impedance at 1 kHz, we saw that the impedance of bare Pt microelectrodes increased significantly following the stimulation (figure 5(E)). Conversely, we found no significant differences in impedances for G-Pt microelectrodes after the stimulation (figure 5(F)), which further demonstrate superior stability of G-Pt microelectrodes.

To better understand the electrochemical characteristics of the microelectrodes, EIS data were fitted to an equivalent circuit model to estimate the parameters of a solution resistance R_s, a charge transfer resistance R_{ct}, a double layer capacitance C_{dl}, a resistance of the adsorbed protein film R_f, capacitance of the protein film C_f, and the Warburg element W (figure 5(G)) [46, 47] (figure 5(G)). Overall, the fractal microelectrodes had lower resistive components (R_s, R_{ct}, and R_f) than circular microelectrodes (table S3). Following the stimulation, we saw substantial changes in each fitted

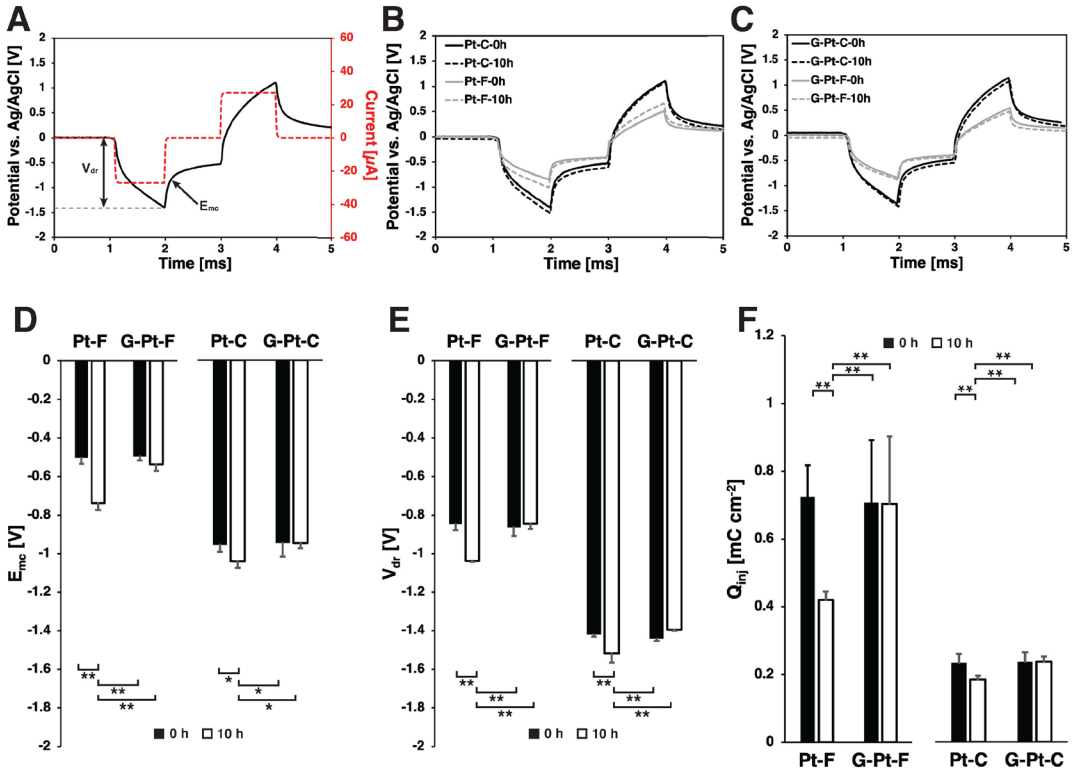

Figure 6. Voltage transients measurement. (A) Representative voltage transient of microelectrode with biphasic, symmetrical current pulse at 50 Hz frequency. (B) Voltage transients from Pt microelectrodes with circular and fractal shape before and after 10 h stimulation. (C) Voltage transients from G-Pt microelectrodes with circular and fractal shape before and after 10 h stimulation. (D) Maximum negative potential excursion. (E) Driving voltage from the microelectrodes. (F) Charge injection limit ($*$ for $p < 0.05$, and $**$ for $p < 0.01$).

parameter for bare Pt microelectrodes. The changes were more pronounced for fractal than circular microelectrodes, which highlight the risk of using unprotected fractal microelectrodes. However, we saw minimal changes across all estimated EIS parameters for the G-Pt microelectrodes after the stimulation.

Interestingly, R_f were higher for bare Pt microelectrodes than G-Pt ones. In contrast, C_f of bare Pt microelectrodes were lower than that of G-Pt microelectrodes. Compared to the surface potential of Pt (<200 mV) [48], the graphene layer has a lower surface potential (−77 mV) in PBS [49], which can electrostatically repulse negatively charged BSA molecules with the surface potential of −20.3 mV in PBS [50]. Therefore, we suspect that there may be a smaller amount of adsorbed protein on Gt-Pt microelectrodes than on bare Pt microelectrodes. Moreover, we saw that the R_f increased while C_f decreased following a 10 h stimulation of bare Pt microelectrodes, which may be due to an increased amount of adsorbed protein. In contrast, we saw little change in R_f and C_f for G-Pt microelectrodes, which suggests there may be relatively little change in protein adsorption amount on these electrodes even after a prolonged neurostimulation.

3.5. Voltage transients

Finally, we compared the voltage transient characteristics of the microelectrodes to confirm the long-term stimulation charge-injection capacity ($n = 5$, each). Each electrode was stimulated using biphasic, symmetric pulses with 1 ms pulse width at 26.97 nC per phase (0.35 mC cm^{-2} with 26.97 μA at 50 Hz). The interphase potential was set to 0 V versus Ag/AgCl reference electrode. To compare, we measured the maximum negative potential excursion (E_{mc}), the maximum driving voltage (V_{dr}), and the charge injection limit (Q_{inj}) from the voltage transient responses (figure 6(A)). Figure 6(B) shows that the maximum negative voltages of both types of bare Pt microelectrodes increased after the 10 h of stimulation. However, G-Pt microelectrodes maintained relatively stable voltage transient responses following the stimulation (figure 6(C)).

The E_{mc} is the potential required to polarize the electrode, which is measured at the end of the cathodic phase of the biphasic pulse. Figures 6(D) and (E) show the comparison of E_{mc} and V_{dr} for each electrode at 26.97 nC per phase. In general, fractal microelectrodes have lower E_{mc} and V_{dr} than the circular ones as we demonstrated previously [17]. Moreover, the bare Pt fractal microelectrodes showed a larger increase in E_{mc} and V_{dr} following 10 h stimulation than the circular microelectrodes, which highlight the design's vulnerability. However, G-Pt microelectrodes showed virtually no change in E_{mc} and V_{dr} following the stimulation.

When comparing the Q_{inj} of each microelectrode, the benefit of G-Pt became even more apparent (figure 6(E)). Our results showed that bare fractal microelectrodes suffered significant loss in Q_{inj} after the 10 h stimulation while G-Pt microelectrodes maintained its Q_{inj}. This bodes well for the high performing fractal designs because their post-stimulation Q_{inj} remained >3X of the circular microelectrodes.

4. Conclusions

From these results, we conclude the following: (1) long-term stimulation of Pt microelectrodes can result in dissolution-induced electrode degradation and failure; (2) fractal microelectrodes have significantly superior charge transfer characteristics than simple circular design; (3) fractal microelectrodes are more susceptible to stimulation-induced dissolution; (4) however, graphene monolayer can significantly reduce the stimulation-induced dissolution in Pt microelectrodes. Taken together, our results suggest that G-Pt fractal microelectrodes may provide an electrochemically more stable interface for neural stimulation. In the future, we plan to verify the long-term reliability and the robustness of these graphene coating and to confirm these finding using *in vitro* and *in vivo* models.

ORCID iDs

Hyunsu Park https://orcid.org/0000-0001-6958-2596
Hyowon Lee https://orcid.org/0000-0001-7628-1441

References

[1] Lockard J S, Congdon W C and DuCharme L L 1990 *Epilepsia* **31** S20–6
[2] Tesfaye S, Watt J, Benbow S J, Pang K A, Miles J and MacFarlane I A 1996 *Lancet* **348** 1698–701
[3] Haberler C, Alesch F, Mazal P R, Pilz P, Jellinger K, Pinter M M, Hainfellner J A and Budka H 2000 *Ann. Neurol.* **48** 372–6
[4] Mayberg H S, Lozano A M, Voon V, McNeely H E, Seminowicz D, Hamani C, Schwalb J M and Kennedy S H 2005 *Neuron* **45** 651–60
[5] Huston J M *et al* 2007 *Crit. Care Med.* **35** 2762–8
[6] Fuentes R, Petersson P, Siesser W B, Caron M G and Nicolelis M A 2009 *Science* **323** 1578–82
[7] Zeitler S, Wendler-Kalsch E, Preidel W and Tegeder V 1997 *Mater. Corros.* **48** 303–10
[8] Donaldson P, Donaldson N N and Brindley G 1985 *Med. Biol. Eng. Comput.* **23** 84–6
[9] Benke G and Gnot W 2002 *Hydrometallurgy* **64** 205–18
[10] Gencoglu A and Minerick A 2009 *Lab chip* **9** 1866–73
[11] De Haro C, Mas R, Abadal G, Muñoz J, Perez-Murano F and Domínguez C 2002 *Biomaterials* **23** 4515–21
[12] Patrick E, Orazem M E, Sanchez J C and Nishida T 2011 *J. Neurosci. Methods* **198** 158–71
[13] Kovach K M, Kumsa D W, Srivastava V, Hudak E M, Untereker D F, Kelley S C, von Recum H A and Capadona J R 2016 *J. Neurosci. Methods* **273** 1–9
[14] Wissel K, Brandes G, Pütz N, Angrisani G L, Thieleke J, Lenarz T and Durisin M 2018 *PLoS One* **13** e0196649
[15] Xu L *et al* 2015 *Adv. Mater.* **27** 1731–7
[16] Watterson W J, Montgomery R D and Taylor R P 2017 *Sci. Rep.* **7** 1–9
[17] Park H, Takmakov P and Lee H 2018 *Sci. Rep.* **8** 1–11
[18] Group GBD 2015 Neurological Disorders Collaborator 2017 *Lancet Neurol.* **16** 877–97
[19] Pikov V 2015 *Global Market for Implanted Neuroprostheses* 1st edn (Sawston: Woodhead Publishing) pp 383–94
[20] Allen M J, Tung V C and Kaner R B 2010 *Chem. Rev.* **110** 132–45
[21] Torrisi F *et al* 2012 *ACS Nano* **6** 2992–3006
[22] Chen H, Müller M B, Gilmore K J, Wallace G G and Li D 2008 *Adv. Mater.* **20** 3557–61
[23] Akinwande D, Tao L, Yu Q, Lou X, Peng P and Kuzum D 2015 *IEEE Nanotechnol. Mag.* **9** 6–14
[24] Brown M A, Barker L, Semprini L and Minot E D 2015 *Environ. Sci. Technol. Lett.* **2** 118–22
[25] Shin S R, Li Y C, Jang H L, Khoshakhlagh P, Akbari M, Nasajpour A, Zhang Y S, Tamayol A and Khademhosseini A 2016 *Adv. Drug Deliv. Rev.* **105** 255–74
[26] Liu N *et al* 2017 *Sci. Adv.* **3** e1700159
[27] Chen S *et al* 2011 *ACS Nano* **5** 1321–7
[28] Kirkland N T, Schiller T, Medhekar N and Birbilis N 2012 *Corros. Sci.* **56**
[29] Prasai D, Tuberquia J C, Harl R R, Jennings G K and Bolotin K I 2012 *ACS Nano* **6** 1102–8
[30] Zhang W *et al* 2014 *Sci. Rep.* **4** 1–8
[31] Shearer C J, Slattery A D, Stapleton A J, Shapter J G and Gibson C T 2016 *Nanotechnology* **27** 1–10
[32] Kang J, Shin D, Bae S and Hong B H 2012 *Nanoscale* **4** 5527–37
[33] Brummer S B and Turner M J 1977 *IEEE Trans. Biomed. Eng.* **BME-24** 440–3
[34] Ahuja A K and Behrend M R 2013 *Prog. Retinal Eye Res.* **36** 1–23
[35] Zhou F, Li Z, Shenoy G J, Li L and Liu H 2013 *ACS Nano* **7** 6939–47
[36] Schriver M, Regan W, Gannett W J, Zaniewski A M, Crommie M F and Zettl A 2013 *ACS Nano* **7** 5763–8
[37] Weatherup R S, D'Arsié L, Cabrero-Vilatela A, Caneva S, Blume R, Robertson J, Schloegl R and Hofmann S 2015 *J. Am. Chem. Soc.* **137** 14358–66
[38] Cui C, Lim A T O and Huang J 2017 *Nat. Nanotechnol.* **12** 834–5
[39] Feng X, Maier S and Salmeron M 2012 *J. Am. Chem. Soc.* **134** 5662–8
[40] Sutter P, Sadowski J T and Sutter E A 2010 *J. Am. Chem. Soc.* **132** 8175–9
[41] Mu R, Fu Q, Jin L, Yu L, Fang G, Tan D and Bao X 2012 *Angew. Chem., Int. Ed. Engl.* **51** 4856–9
[42] Wintterlin J and Bocquet M 2009 *Surf. Sci.* **603** 1841–52
[43] Batzill M 2012 *Surf. Sci. Rep.* **67** 83–115
[44] Yao Y *et al* 2014 *Proc. Natl Acad. Sci.* **111** 17023–8
[45] Knoch J, Chen Z and Appenzeller J 2012 *IEEE Trans. Nanotechnol.* **11** 513–9
[46] Diniz F B, Ueta R R, Pedrosa A M C, Areias M D C, Pereira V R, Silva E D, Da Silva J G, Ferreira A G and Gomes Y M 2003 *Biosens. Bioelectron.* **19** 79–84
[47] Macdonald M A and Andreas H A 2014 *Electrochim. Acta* **129** 290–9
[48] Héduit A, Quinio I, Stadmuller D and Thévenot D R 1996 *Water Sci. Technol.* **34** 143–50
[49] Parra C, Dorta F, Jimenez E, Henríquez R, Ramírez C, Rojas R and Villalobos P 2015 *J. Nanobiotechnol.* **13** 1–10
[50] Li R, Wu Z, Wangb Y, Ding L and Wang Y 2016 *Biotechnol. Rep.* **9** 46–52